Shared-Receiver Battery Equalizer Based on Inductive Power Transfer and Bidirectional DC-DC Converter

Yinqin Liao, Student Member, IEEE, Xinzhi Zhang, Long Chen, Student Member, IEEE, Feiliang Li, Chunsheng Wang, Member, IEEE, Yuan Cao, Member, IEEE, and Yukun Hu, Senior Member, IEEE

Abstract—State-of-charge (SOC) balancing is essential for safe, reliable, and long-lived operation of battery energy storage operation. Conventional wired equalizers are hampered by permanent physical connections, limited flexibility, and heightened safety hazards. To address these limitations, an inductive power transfer (IPT)-based equalizer is introduced in this article, in which the singleinductor DC-DC converter's inductor is replaced by a transmitter coil to wirelessly transfer ripple energy for SOC balancing during both charging and discharging. Additionally, a single receiver coil and switch matrix are employed, shared sequentially among all cells with adaptive connection intervals regulated by a presented efficient adaptive equalization algorithm. The equalization performance is analyzed and validated using a downscaled proof-of-concept prototype. Furthermore, the tradeoff between balancing capability and efficiency is discussed, along with the potential for cell-level fault isolation at a slightly improvement on topology.

Index Terms—Battery balancing, energy storage system, state-of-charge, inductive power transfer.

I. INTRODUCTION

Lithium-Ion batteries, as representatives of energy storage systems, are extensively employed in electric vehicles (EVs), smart grids, consumer electronics, and other applications due to their advantages of high energy density, long lifespan, and no memory effect, etc. [1]–[3]. In general, lithium-ion battery cells are generally connected in series or parallel to meet high voltage or power requirements [4]. However, variations in charging and discharging rates can arise due to differences in fabrication parameters, state-of-health (SOH), and ambient temperature, leading to state-of-charge (SOC) imbalances [5]. These SOC discrepancies not only pose potential fire and explosion hazards during charging but can also cause irreversible battery damage during discharging, resulting in a shortened battery lifespan [6].

Battery equalization is essential for prolonging the lifespan

This work was supported in part by the National Natural Science Foundation (NNSF) of China under Grant 62103443, in part by the Hunan Natural Science Foundation under Grant 2022JJ40630, and in part by the Fundamental Research Funds for the Central Universities of Central South University under Grant 2025ZZTS0734. (Corresponding author: Yuan Cao.)

Yinqin Liao, Xinzhi Zhang, Long Chen, Feiliang Li, Chunsheng Wang, and Yuan Cao are with the School of Automation, Central South University, Changsha 410083, China (e-mail: liao_yinqin@csu.edu.cn; 244612238@csu.edu.cn; chend1729@csu.edu.cn; csu_xffl@csu.edu.cn; wangcsu@csu.edu.cn; caoyuan3116@csu.edu.cn).

Yukun Hu is with the Department of Civil, Environment and Geomatic Engineering, University College London, London WC1E 6BT, U.K. (e-mail: yukun.hu@ucl.ac.uk).

and improving the safety of series-connected lithium-ion cells. Numerous equalizer topologies have been developed and can be broadly categorized into passive and active approaches [7]. Passive methods are favored for their simplicity and low cost [8], but they dissipate excess energy as heat, leading to thermal management challenges. Active equalizers, on the other hand, redistribute charge among cells using external circuits based on switched capacitors [9], inductors [10], DC–DC converters [11], [12], transformers [13]–[18] or wireless power transfer (WPT) [19]–[27].

Among these, transformer-based equalizers remain popular due to their high energy efficiency and electrical isolation. However, reliance on iron cores induces bulky designs, raises material costs and introduces safety concerns such as core saturation, overheating and fault risks [19], [23]. These core-related limitations motivate the exploration of WPT-based equalizers, which offer contactless, coreless energy transfer and thereby improve safety, flexibility, and modularity.

Recent WPT-based equalizers can be categorized into multi-receiver and single-receiver architectures. Multi-receiver systems, such as the megahertz-range design presented in [19], allow simultaneous balancing of multiple cells but require a full-bridge rectifier and a dedicated receiver (Rx) coil per cell, increasing component count and cost. To address this, [20] employs the voltage doublers, which reduces the number of required diodes and Rx coils by half. Further reduction is achieved in the modular equalizer proposed in [21], which minimizes the number of Rx coils under similar operating conditions as in [19]. Additionally, a dual-layer receiver architecture in [22] enhanced anti-misalignment capability in multi-receiver systems. Nevertheless, cross-coupling between coils and inconsistent parameters of Rx coils can still degrade balancing performance [28].

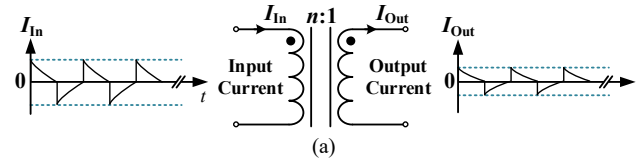
To overcome these drawbacks, single-receiver architectures have been introduced. In [23], a voltage equalizer (VE) with a single Rx coil enables cell balancing during charging, but integrated voltage multiplier (VM) topology suffers from low conversion efficiency [29]. To improve this, [24] introduces a hybrid switching strategy that alternates between VE and a rectifier bridge to reduce conduction losses. Furthermore, switch-matrix-based designs in [25] achieve higher efficiency active balancing without relying on VM topologies.

Despite their advantages, most existing WPT-based battery equalizers are limited in operational flexibility. For instance, [26] supports balancing only during idle states, [19]–[25] operate solely during charging due to their reliance on external AC sources or internal inverters, and [27] functions only during discharging by utilizing current ripple. Such single-

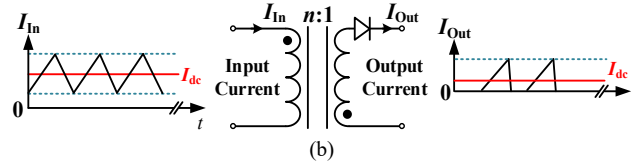
direction operation allows SOC differences in the other mode to accumulate, leading to large deviations when switching between charging and discharging, which can destabilize balancing control and increase the risk of overcharge or overdischarge, potentially causing capacity loss, thermal runaway, or even safety failures [6].

To fill this gap, an inductive power transfer (IPT)-based equalizer capable of bidirectional balancing during charging and discharging is introduced in this work. Although both transformers and IPT systems utilize magnetic induction, their operating principles are completely different. To clarify these differences, Fig. 1 shows the configurations of a transformer method, a coupled inductors method, a classical WPT system, and the IPT method employed in this work.

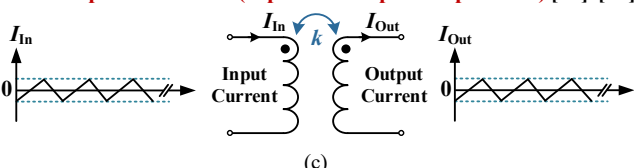
Transformer (Input and output are pure AC) [13]



Inversely coupled power inductor [14]–[18] (Input and output currents are DC current with AC ripple)



Wireless power transfer (Input and output are pure AC) [19]-[26]



Iuductive power transfer employed in this paper [27], [30] (Input current is DC current with AC ripple, and output is pure AC)

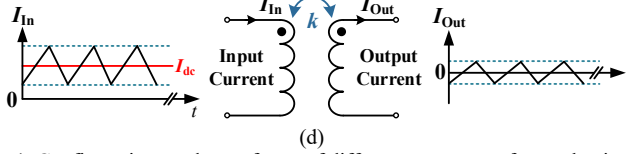


Fig. 1. Configurations and waveforms of different power transfer mechanisms. (a) Conventional transformer. (b) Coupled inductor (flyback converter). (c) Wireless power transfer. (d) Employed inductive power transfer method.

In Fig. 1(a), the conventional transformer consists of tightly coupled windings on a shared magnetic core. Both primary and secondary currents are purely AC with zero average value, and energy transfer occurs instantaneously via magnetic coupling. In contrast, this coupled inductor configuration allows for input and output currents with nonzero average values, comprising a DC component with AC ripple, as shown in Fig. 1(b). The presence of a magnetic core is essential to its energy transfer mechanism, as it enables energy storage during the switching intervals.

Fig. 1(c) shows a classical WPT system based on air-core coils, where both the Tx and Rx carry pure AC currents. WPT methods can generally be categorized into magnetic resonance (MR) and IPT. MR systems typically operate in resonant and support long-distance power transfer, whereas IPT systems are mostly non-resonant and designed for mid-range transfer.

Finally, Fig. 1(d) depicts the IPT-based method employed in this work. The input current contains a DC component with AC ripple, while the output current exhibits a purely AC.

From a waveform perspective, the presented method does not exactly match any of the conventional categories above. However, it differs fundamentally from the coupled inductor method in that it does not incorporate and rely on a magnetic core. Despite lacking strict electrical isolation, the presented method shares key IPT characteristics such as contactless energy transfer, physical removability, and magnetic coupling via air-core coils. Therefore, the presented method is most appropriately classified as a variant of IPT.

Besides, a notable limitation of the presented topology is that the Tx coil in the employed topology must handle a large current ripple to deliver balancing energy, which may impose additional ripple stress on components and lead to increased conduction losses. Nevertheless, the overall system stability and the operation of the main circuit remain unaffected. The key contributions of this work are given as follows:

- 1) An IPT-based battery equalizer is developed by replacing the inductor in a bidirectional converter with a Tx coil. By multiplexing the AC and DC components in the Tx coil current, wireless battery balancing is enabled during both charging and discharging processes.
- 2) To enable the single receiver structure, a switch matrix is introduced in this work, which eliminates cross-coupling issues associated with multi-receiver configurations and provides the potential for bypassing faulty cells.
- 3) In this work, an efficient adaptive equalization algorithm, incorporating a connection duration controller, is presented to ensure accurate balancing and to minimize overall power losses during the equalization process.

The rest of this paper is arranged as follows: Section II introduces the configuration and fundamental operating principles of the enhanced IPT-based battery equalizer. Section III details the control strategy. Experimental validation using a scaled-down prototype is presented in Section IV. Section V provides additional comments and insights on the presented method, followed by a comparative evaluation with existing equalizers in Section VI. Finally, conclusions are summarized in Section VII.

II. FUNDAMENTAL ANALYSIS

This section elaborates on the configuration of the presented battery equalizer, comprising a bi-directional single-inductor DC-DC converter and a balancing circuit. Moreover, the direction of current is analyzed in both the charging and discharging processes, and both are divided into four operation stages in a switching period of the converter.

A. Structure of IPT-Based Equalizer

Fig. 2 shows the configuration of the presented IPT-based equalizer, which integrates a bidirectional single-inductor DC-DC converter (represented by the black line) with a balancing circuit (represented by the blue line).

The converter comprises two complementary MOSFETs, S_H and S_L , an inductor L_{Tx} , and filter capacitors C_L and C_H . The right side of the converter is connected to a series of n battery cells, while the left side is connected to the rest of the system, including power sources for charging or loads for discharging.

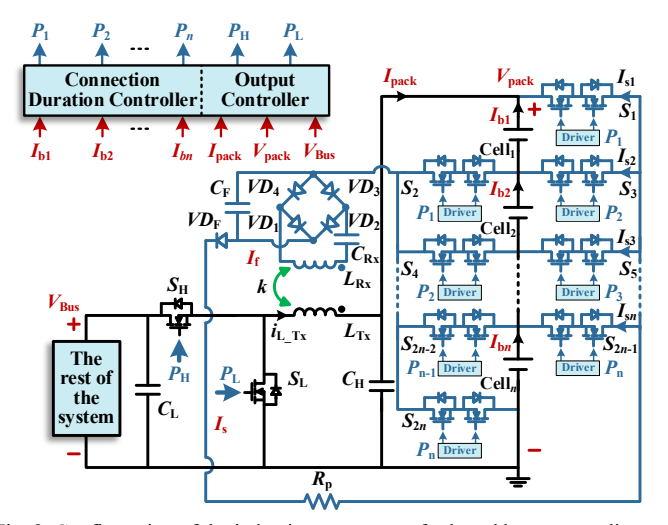


Fig. 2. Configuration of the inductive power transfer-based battery equalizer.

Building on the introduced bi-directional single-inductor DC-DC converter, a balancing circuit is incorporated to enable the IPT process. In this circuit, the inductor L_{Tx} within the converter functions as a Tx coil for IPT. A single Rx coil L_{Rx} , is coupled with L_{Tx} to wirelessly receive feedback energy via a coupling coefficient k. Diodes VD_1-VD_4 form a rectifier bridge following L_{Rx} , which is connected to a filter capacitor C_F to prevent a rapid drop in Rx current. Additionally, a diode $VD_{\rm F}$ is placed after $C_{\rm F}$ to ensure unidirectional feedback current. The switch matrix, which is composed of dual nchannel common source MOSFETs as the sequential cell switches S_1-S_{2n} , directs wireless energy to the selected battery cell, with details control strategy provided in Section III.

B. Discharging Mode

For the single Tx and single Rx system, the coupling efficiency k is typically high enough to ensure rectifier bridge conduction through proper design of the inductances, shape, and size of the coils. However, if k is extremely low, meaning the coils are barely coupled, the system naturally operates as a conventional converter, with the Rx side left open-circuited and no energy received.

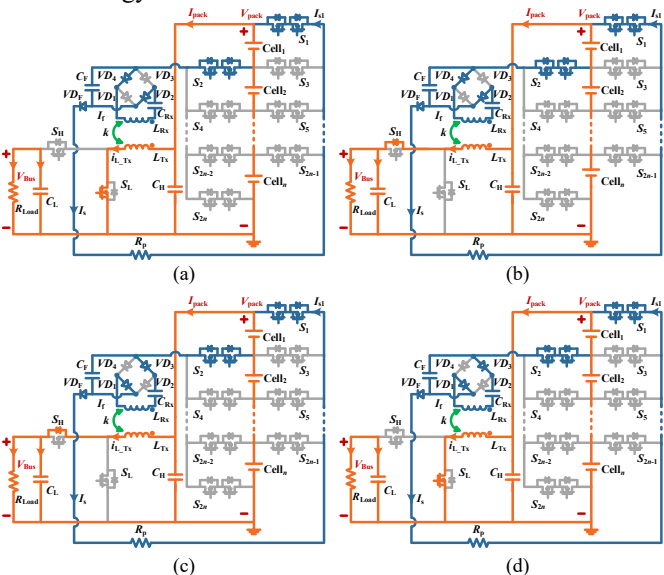


Fig. 3. Operating states during discharging mode. (a) State 1. (b) State 2. (c) State 3. (d) State 4.

When a load is connected to the left side of the presented bi-directional single-inductor DC-DC converter, the converter operates as a boost converter to discharge the battery pack. The load voltage is regulated by the duty cycle D_L of switch $S_{\rm L}$. Using closed-loop control, the duty cycle $D_{\rm L}$ is adjusted to maintain a constant load voltage, denoted as $V_{\rm Bus}$.

For example, when the first battery cell Cell₁ is selected, the converter's operation during discharging divides the switching period T_0 into four states based on the state and direction of the current I_{Tx} flowing through L_{Tx} , as shown in Fig. 3. It is worth to highlight that during the entire discharging process, the current I_{Tx} consistently flows through L_{Tx} from right to left, which is defined as negative.

1) State 1 (t_1-t_2) : As shown in Fig. 3(a), when the S_L is turned on, current I_{Tx} flows through L_{Tx} with a raised absolute magnitude. A positive voltage is induced to the left of L_{Rx} , thereby increasing the feedback current I_f flowing through from left to right, rendering VD_2 and VD_4 of the rectifier bridge conductive. By utilizing Kirchhoff's voltage law (KVL) in both the converter and balancing circuits, (1) can be derived. It is worth noting that while the diode drop is considered in the balancing loop (Rx side), it is neglected in the converter circuit (Tx side) due to the significantly higher voltage level of the converter.

$$\begin{cases} V_{\text{Tx}_{\text{D}1}} = -\frac{M}{L_{\text{Rx}}} V_{\text{Rx}_{\text{D}1}} - V_{\text{pack}} \\ V_{\text{Rx}_{\text{D}1}} = -\frac{M}{L_{\text{Tx}}} V_{\text{Tx}_{\text{D}1}} - V_{\text{drop}} - V_{\text{F}} \end{cases}$$

$$(1)$$

where $V_{\text{Tx D1}}$ and $V_{\text{Rx D1}}$ denote the voltages across L_{Tx} and L_{Rx} in State 1, respectively. V_{pack} represents the voltage of the battery pack. Additionally, V_F represents the terminal voltage of filter capacitor C_F , and V_{drop} denotes the total voltage drop across the IPT loop, including the rectifier. In this section, the reference direction for the voltages V_{Tx} and V_{Rx} is defined as left positive and right negative.

According to (1), $V_{\text{Tx D1}}$ and $V_{\text{Rx D1}}$ in the **State 1** during discharging mode can be solved as

$$\begin{cases} V_{\text{Tx}_\text{D1}} = -\frac{L_{\text{Tx}} \left(L_{\text{Rx}} V_{\text{pack}} - M (V_{\text{F}} + V_{\text{drop}}) \right)}{L_{\text{Tx}} L_{\text{Rx}} - M^2} \\ V_{\text{Rx}_\text{D1}} = \frac{L_{\text{Rx}} \left(M V_{\text{pack}} - L_{\text{Tx}} (V_{\text{F}} + V_{\text{drop}}) \right)}{L_{\text{Tx}} L_{\text{Rx}} - M^2} \end{cases}$$
(2)

2) State 2 (t_2-t_3) : As shown in Fig. 3(b), when the S_L is deactivating, the battery pack charges the load with a reduced absolute current I_{Tx} , maintaining the same direction as in **State** 1. A positive voltage is generated on the right side of L_{Rx} . However, due to the presence of L_{Tx} , the current flowing through L_{Tx} cannot be reversed immediately. The following KVL equation can be obtained as

$$\begin{cases} V_{\text{Tx}_D2} = -\frac{M}{L_{\text{Rx}}} V_{\text{Rx}_D2} + V_{\text{Bus}} - V_{\text{pack}} \\ V_{\text{Rx}_D2} = -\frac{M}{L_{\text{Tx}}} V_{\text{Tx}_D2} - V_{\text{drop}} - V_{\text{F}} \end{cases}$$
(3)

Therefore, $V_{\text{Tx D2}}$ and $V_{\text{Rx D2}}$ in **State 2** can be described as

Therefore,
$$V_{\text{Tx}} = \frac{1}{D_2} \text{ and } V_{\text{Rx}} = \frac{1}{D$$

From (4), it is evident that the $V_{\rm Rx_D2}$ assumes a negative value, causing the feedback current $I_{\rm f}$ to diminish, flowing from left to right. As $I_{\rm f}$ drops to zero, **State 2** ends.

3) State 3 (t_3 – t_4): The switch S_L remains in the turned-off state as depicted in Fig. 3(c), indicating that the direction of the induced voltage across $L_{\rm Rx}$ remains the same as in State 2. However, after the current reset following State 2, the current flowing through $L_{\rm Tx}$ reverses its direction (from right to left), resulting in the conduction of VD_1 and VD_3 in the rectifier. The KVL equation can be given as

$$\begin{cases} V_{\text{Tx}_{D3}} = -\frac{M}{L_{\text{Rx}}} V_{\text{Rx}_{D3}} + V_{\text{Bus}} - V_{\text{pack}} \\ V_{\text{Rx}_{D3}} = -\frac{M}{L_{\text{Tx}}} V_{\text{Rx}_{D3}} + V_{\text{drop}} + V_{\text{F}} \end{cases}$$
(5)

Through the resolution of (5), V_{Tx_D3} and V_{Rx_D3} in **State 3** can be denoted as

$$\begin{cases} V_{\text{Tx}_{\text{D}3}} = \frac{L_{\text{Tx}} \left(L_{\text{Rx}} (V_{\text{Bus}} - V_{\text{pack}}) - M (V_{\text{F}} + V_{\text{drop}}) \right)}{L_{\text{Tx}} L_{\text{Rx}} - M^{2}} \\ V_{\text{Rx}_{\text{D}3}} = -\frac{L_{\text{Rx}} \left(M (V_{\text{Bus}} - V_{\text{pack}}) - L_{\text{Tx}} (V_{\text{F}} + V_{\text{drop}}) \right)}{L_{\text{Tx}} L_{\text{Rx}} - M^{2}} \end{cases}$$
(6)

4) State 4 (t_4 – t_5): As shown in Fig. 3(d), upon activating the S_L , L_{Rx} is charged by the battery pack with an increased current. The induced voltage on the Rx side is positive left, while the current flowing through L_{Tx} maintains its direction as in **State 3**. This process can be characterized as

$$\begin{cases} V_{\text{Tx}_{D4}} = -\frac{M}{L_{\text{Rx}}} V_{\text{Rx}_{D4}} - V_{\text{pack}} \\ V_{\text{Rx}_{D4}} = -\frac{M}{L_{\text{Tx}}} V_{\text{Tx}_{D4}} + V_{\text{drop}} + V_{\text{F}} \end{cases}$$
(7)

By deriving solutions from (7), V_{Tx_D4} and V_{Rx_D4} in **State 4** can be expressed as

$$\begin{cases} V_{\text{Tx_D4}} = -\frac{L_{\text{Tx}} \left(L_{\text{Rx}} V_{\text{pack}} + M (V_{\text{F}} + V_{\text{drop}}) \right)}{L_{\text{Tx}} L_{\text{Rx}} - M^{2}} \\ V_{\text{Rx_D4}} = \frac{L_{\text{Rx}} \left(M V_{\text{pack}} + L_{\text{Tx}} (V_{\text{F}} + V_{\text{drop}}) \right)}{L_{\text{Tx}} L_{\text{Rx}} - M^{2}} \end{cases}$$
(8)

As shown in (8), it is apparent that the $V_{\rm Rx_D4}$ returns to a positive value, prompting the resetting of the feedback current $I_{\rm f}$, which flows from right to left. Once $I_{\rm f}$ reaches zero, **State 4** ends and **State 1** is restarted, marking the initiation of a new converter switching period T_0 .

C. Charging Mode

When a high-voltage power source is connected to the input of the converter on the left side, the converter operates in charging mode, functioning as a buck converter. Similarly, the voltage of a high-power DC source is represented as $V_{\rm Bus}$. The charging voltage and current are determined by the duty cycle $D_{\rm H}$ of switch $S_{\rm H}$. The constant current constant voltage (CCCV) charging strategy is employed for battery protection.

In the discharging mode, the system manifests four operating states within a converter switching period T_0 , as shown in Fig. 4 with a relatively high coupling efficiency k. Although the current $I_{\rm Tx}$ through inductor $L_{\rm Tx}$ flows in opposite directions during charging compared to discharging, the current loop structure remains similar in both modes. Consequently, the KVL equations derived for the discharging process are also applicable during charging, resulting in

analogous expressions for V_{Tx} and V_{Rx} , as derived from (2), (4), (6), and (8).

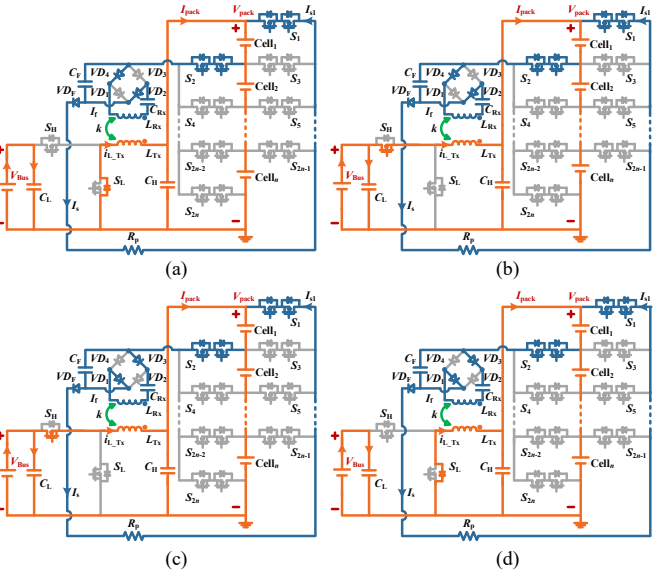


Fig. 4. Operating states during charging mode. (a) *State 1*. (b) *State 2*. (c) *State 3*. (d) *State 4*.

D. Operating Principle of the Balancing Switch Matrix

To accommodate a single Rx coil configuration, a switch matrix is employed to sequentially connect the Rx circuit to each individual battery cell. This subsection illustrates how the switch matrix coordinates with the Rx coil to enable cell balancing under different operating states.

As an illustrative example, Fig. 5 shows the current flow paths during *State 1* of the discharging mode in a four-cell pack. Although different combinations of switches are activated depending on the selected cell, the resulting current loops follow a consistent structural pattern, ensuring the balancing mechanism functions uniformly across all cells.

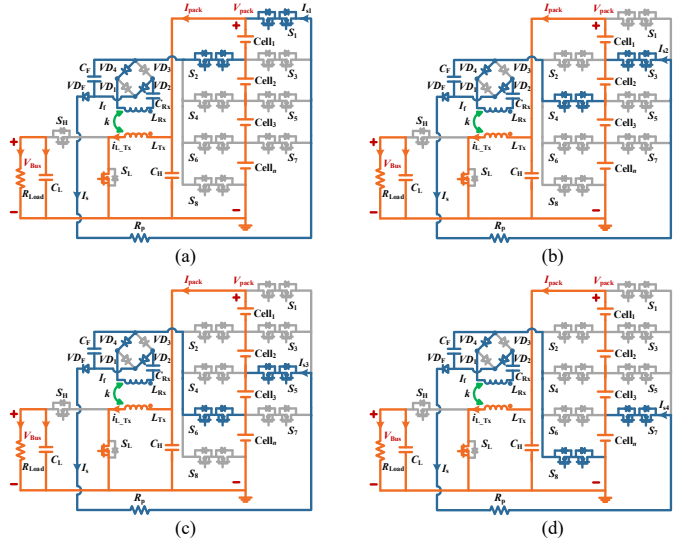


Fig. 5. Current flow paths in *State 1* during discharging. (a) Cell₁ is selected. (b) Cell₂ is selected. (c) Cell₃ is selected. (d) Cell₄ is selected.

To further clarify the operating principle of switch matrix, the turned-on switch combinations for each state and selected cell are summarized in TABLE I. This switching strategy ensures that each cell can be individually connected for balancing without interference or cross-coupling.

TABLE I TURNED-ON SWITCHES FOR EACH BALANCING STATE AND CELL CONNECTION IN A FOUR-CELL PACK

	Cell ₁	Cell ₂	Cell ₃	Cell ₄
State 1	S_L , S_1 , and S_2	S_L , S_3 , and S_4	S_L , S_5 , and S_6	S_L , S_7 , and S_8
State 2	S_H , S_1 , and S_2	S_H , S_3 , and S_4	$S_{\rm H}$, $S_{\rm 5}$, and $S_{\rm 6}$	$S_{\rm H}$, $S_{\rm 7}$, and $S_{\rm 8}$
State 3	$S_{\rm H}$, $S_{\rm 1}$, and $S_{\rm 2}$	$S_{\rm H}$, $S_{\rm 3}$, and $S_{\rm 4}$	$S_{\rm H}$, $S_{\rm 5}$, and $S_{\rm 6}$	$S_{\rm H}$, $S_{\rm 7}$, and $S_{\rm 8}$
State 4	S_L , S_1 , and S_2	S_L , S_3 , and S_4	S_L , S_5 , and S_6	S_L , S_7 , and S_8

It is worth noting that although the switching structure remains the similar across different cell selections, the actual current values vary depending on the terminal voltage of the connected cell. Detailed analysis of the feedback current, shunt current, and control strategy is provided in Section III.

III. DISCUSSION OF THE BALANCING STRATEGY

In this section, the relationship between the feedback current and the voltage of the filter capacitors is analyzed and discussed. Based on this analysis, an efficient adaptive equalization algorithm is introduced, which allocates the connection duration for each battery cell.

A. Analysis of the Feedback Current

Both the discharging and charging modes demonstrate that $V_{\rm TX}$ and $V_{\rm RX}$ exhibit analogous behavior within the same operational state in each mode. As a result, the principal waveforms of the PWM signals for S_L, S_H, the feedback current I_f , Tx coil's current I_{Tx} (defined as negative), and the voltage V_{RX} of the Rx coil during discharging are shown as an example in Fig. 6.

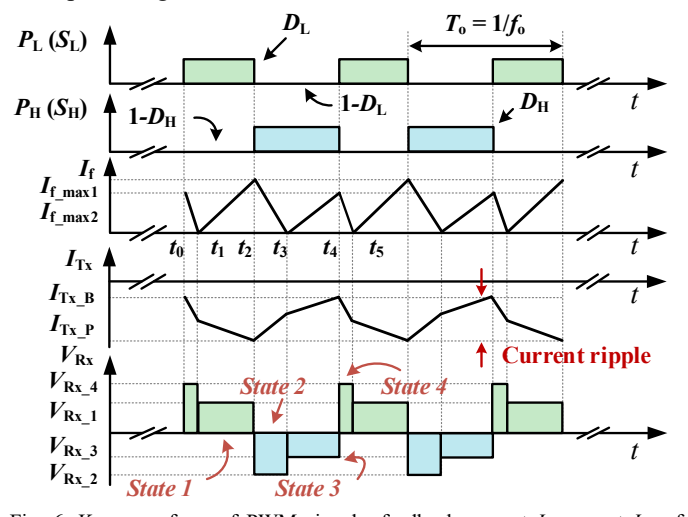


Fig. 6. Key waveform of PWM signals, feedback current I_f , current I_{Tx} of transmitter coil, and voltage V_{RX} of receiver coil in discharging mode.

From Fig. 6, with t_0 defined as the initial time and set to zero, the relationship among t_2 , t_4 , D_H , D_L , and T_0 can be given as

$$t_2 = D_L T_o = (1 - D_H) T_0$$
 (9)
 $t_4 = T_0$ (10)

where T_0 is the switching period of the converter. Assuming the system reaches a steady state, (11) and (12) are derived based on the inductor volt-second balance principle.

$$(t_2 - t_1) \times V_{\text{Rx D1}} + (t_3 - t_2) \times V_{\text{Rx D2}} = 0$$
 (11)

$$(t_4 - t_3) \times V_{\text{Rx D3}} + (t_5 - t_4) \times V_{\text{Rx D4}} = 0.$$
 (12)

In steady-state conditions, the duration from t_4 to t_5 is equal to the interval from t_0 to t_1 . When the converter circuit operates in continuous current mode (CCM), the time intervals from t_0 to t_4 satisfy

$$0 = V_{\text{Tx_D1}}(t_2 - t_1) + V_{\text{Tx_D2}}(t_3 - t_2) + V_{\text{Tx_D3}}(t_4 - t_3) + V_{\text{Tx_D4}}(t_5 - t_4).$$
(13)

$$t_1 = T_0 \frac{D_L M V_{\text{pack}} - L_{\text{Tx}} D_{\text{H}} (V_{\text{F}} + V_{\text{drop}})}{2M V_{\text{pack}}}$$
(14)

$$+V_{\text{Tx_D3}}(t_4 - t_3) + V_{\text{Tx_D4}}(t_5 - t_4).$$
Combining (11)–(13), t_1 , t_3 , and V_{Bus} can be resolved as
$$t_1 = T_0 \frac{D_L M V_{\text{pack}} - L_{\text{Tx}} D_{\text{H}}(V_{\text{F}} + V_{\text{drop}})}{2M V_{\text{pack}}}$$

$$t_3 = T_0 \frac{(1 + D_L) M V_{\text{pack}} - L_{\text{Tx}} D_{\text{H}}(V_{\text{F}} + V_{\text{drop}})}{2M V_{\text{pack}}}$$

$$V_{\text{Bus}} = \frac{V_{\text{pack}}}{D_H} = \frac{V_{\text{pack}}}{1 - D_L}.$$
(15)
As shown in (16), although energy is transmitted back to the

$$V_{\text{Bus}} = \frac{V_{\text{pack}}}{D_H} = \frac{V_{\text{pack}}}{1 - D_L}.$$
 (16)

As shown in (16), although energy is transmitted back to the battery pack through IPT, the output characteristics of the bidirectional DC-DC converter, whether operating in buck or boost mode, remain unaffected.

According to (14) and (15), the current ripple ΔI_{Tx} of Tx coil (converter's inductor) in the presented equalizer can be

$$\Delta I_{\text{Tx}} = \frac{V_{\text{Tx}}D2}}{L_{\text{Tx}}} (t_3 - t_2) + \frac{V_{\text{Tx}}D3}}{L_{\text{Tx}}} (t_4 - t_3)$$

$$= \frac{T_0 (L_{\text{Rx}}V_{\text{pack}}(V_{\text{Bus}} - V_{\text{pack}}) - L_{\text{Tx}}(V_{\text{F}} + V_{\text{drop}})^2)}{V_{\text{Bus}}(L_{\text{Tx}}L_{\text{Rx}} - M^2)}$$
(17)

Furthermore, $I_{f \text{ max}1}$ and $I_{f \text{ max}2}$ can be derived as

$$I_{f_{-}max1} = V_{Rx_{-}D1}(t_2 - t_1)$$
 (18)

$$I_{\text{f_max2}} = V_{\text{Rx_D3}}(t_4 - t_3).$$
 (19)

Ultimately, the average feedback current $I_{f ave}$ could be

$$I_{f_{\text{ave}}} = \frac{I_{f_{\text{max1}}}(t_3 - t_1) + I_{f_{\text{max2}}}(t_1 + t_4 - t_3)}{2T_0}.$$
 (20)

By substituting equations (14) through (19) into (20), equation (21) is derived, where f_0 represents the switching frequency of the converter. It is evident that the average feedback current $I_{\rm f}$ ave is inversely proportional to f_0 .

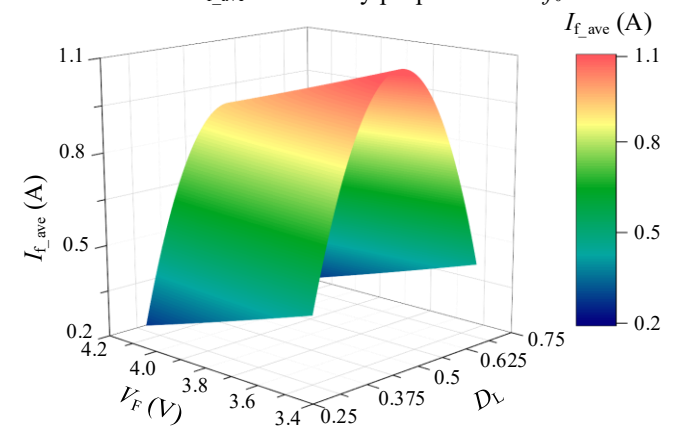


Fig. 7. 3D plot of $I_{\rm f}$ ave as a function of filter capacitor voltage $V_{\rm F}$ and duty cycle $D_{\rm L}$ based on the parameters listed in Table I.

$$I_{\text{f_ave}} = \frac{\left(D_{\text{H}}MV_{\text{Bus}} - L_{\text{Tx}}(V_{\text{F}} + 2V_{\text{drop}})\right) \times \left(D_{\text{H}}D_{\text{L}}MV_{\text{Bus}} - L_{\text{Tx}}D_{\text{H}}(V_{\text{F}} + 2V_{\text{drop}})\right)}{4f_{\text{O}}MD_{\text{H}}V_{\text{Bus}}(L_{\text{Tx}}L_{\text{By}} - M^{2})}$$
(21)

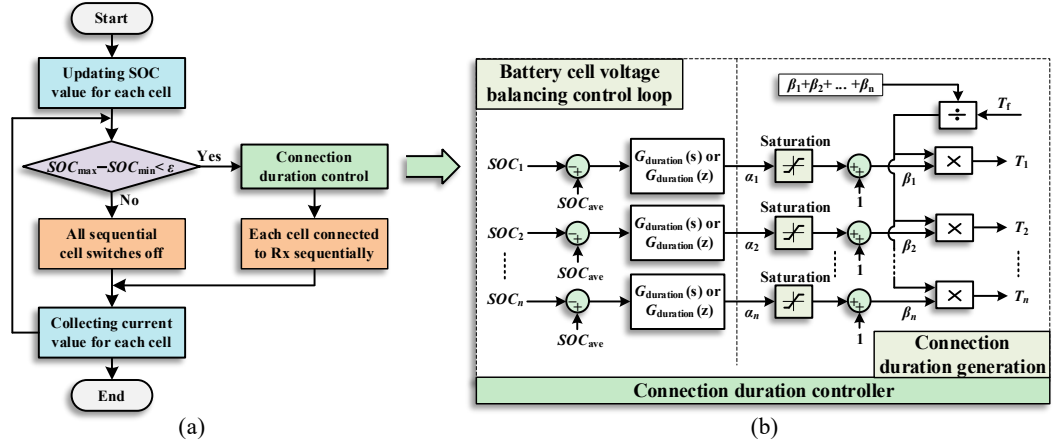


Fig. 8. State-of-charge equalization control strategy. (a) The introduced efficient adaptive equalization algorithm. (b) The connection duration controller.

TABLE II PARAMETERS USED TO CALCULATE AVERAGE FEEDBACK CURRENT IN FIG. 6

Symbol	Value	Symbol	Value
f_0	200 kHz	L_{Tx}	12.7 μΗ
$V_{ m Bus}$	38 V	$L_{ m Rx}$	$10 \mu\mathrm{H}$
k	0.82	$D_{ m L}$	0.25 - 0.75
$V_{ m drop}$	0.7 V	$V_{ m F}$	2.75-4.2 V

To further investigate the relationship between $I_{\rm f}$ ave, $D_{\rm L}$, and $V_{\rm F}$, the values of $I_{\rm f}$ ave corresponding to different terminal voltages V_F of the filter capacitor C_F and D_L are calculated using the parameters listed in TABLE II, as shown in Fig. 7.

As illustrated in Fig. 7, a lower V_F leads to a higher average feedback current If ave, indicating that more energy is transferred back to the lower-voltage battery cell over the same period. Furthermore, as the duty cycle D_L approaches 0.5, the average feedback current increases, peaking at 1.124 A when V_F is 3.4V and D_L is 0.5. Additionally, the dynamic

equation of
$$V_{\rm F}$$
 can be represented as
$$C_{\rm F} \frac{dV_{\rm F}}{dt} = I_{\rm f_ave} - I_{\rm si} = I_{\rm f_ave} - \frac{V_{\rm F} - V_{\rm bi} - V_{\rm d}}{R_{\rm p}} \tag{22}$$

where I_{si} and V_{bi} represent the shunt current and terminal voltage of the *i*-th battery cell, respectively, $V_{\rm d}$ is the forward voltage drop of diode VD_F , and R_P is the parasitic resistance.

It is observed that as V_{bi} increases, V_F increases accordingly, leading to a reduced average feedback current $I_{f ave}$. This reduction in $I_{f \text{ ave}}$ results in a lower shunt current I_{si} in the steady state. Thus, higher values of V_{bi} are associated with decreased values of both I_{f} ave and I_{si} in the steady state.

B. Introduction of the Adaptive Equalization Algorithm

Although the negative relationship is provided in the last subsection, the equalization speed seems slow if it depends on a constant connection duration for all cells. To address this, an efficient adaptive equalization algorithm is introduced for a battery pack with n cells, as shown in Fig. 8(a).

At the beginning of each cycle, the SOC values for each cell are updated. If the difference between the maximum SOC (SOC_{max}) and the minimum SOC (SOC_{min}) is below a specified threshold δ , the system is considered balanced. Consequently, all cell switches are deactivated, halting the IPT process to improve overall efficiency.

Conversely, if the difference between SOC_{max} and SOC_{min} exceeds the threshold δ , the system is seen as being in an imbalanced condition. In this case, the connection duration

controller adjusts the connection times for each cell based on its SOC value, as illustrated in Fig. 8(b). Each cell is sequentially connected to the Rx for an adaptive duration within a constant total cycle time $T_{\rm f}$. Finally, the discharging or charging current of each cell is measured to update the SOC values for the subsequent cycle.

To reach effective balancing, the connection duration

controller calculates the average SOC value, which is given as
$$SOC_{\text{ave}} = \frac{\sum_{i=1}^{n} SOC_{i}}{n} \times 100\%$$
(23)

where SOC_i represents the SOC of the *i*-th cell. The deviations between SOC_i and SOC_{ave} are processed by the duration compensator, which is represented by the continuous-time function $G_{\text{duration}}(s)$ or the discrete-time transfer function $G_{\text{duration}}(z)$. In this paper, $G_{\text{duration}}(z)$ is utilized and defined as

$$G_{\text{duration}}(z) = K_{\text{P_duration}} + \frac{K_{\text{I_duration}}}{z - 1}$$
 (24)

where $K_{\rm P}$ duration and $K_{\rm I}$ duration are the proportional and integral gains, respectively. The output α_i of the *i*-th duration compensator is processed through a saturation module, and the duration multiplier β_i for the *i*-th battery cell can be given as

$$\beta_{i} = \begin{cases} 0, & \alpha_{i} < -1\\ \alpha_{i} + 1, & -1 \le \alpha_{i} \le 1\\ 2, & \alpha_{i} > 1 \end{cases}$$
 (25)

Based on the computed duration multipliers β_1 to β_n , the connection duration T_i for the i-th battery cell can be given as

$$T_i = \frac{\beta_i}{\sum_{i=1}^n \beta_i} \times T_f \tag{26}$$

where $T_{\rm f}$ denote the predefined constant total cycle time of the switch matrix.

As an expanded view of Fig. 6, Fig. 9 depicts the switching signals of cell switches S_1 - S_4 , the low-side switch drive signal $S_{\rm L}$, the inductor current $I_{\rm Tx}$, the feedback current $I_{\rm f}$, and the shunt currents I_{s1} and I_{s2} during discharging as an instance.

The controller assigns longer connection intervals to cells with lower SOC and shorter intervals to those with higher SOC. Specifically, when balancing the *i*-th cell, switches S_{2i-1} and S_{2i} in the switch matrix are turned on to connect this cell to the balancing circuit. Moreover, as derived in (20), a cell with higher SOC exhibits an elevated terminal voltage, which in turn reduces its feedback and shunt currents. By leveraging the intrinsic behavior of the equalizer topology together with the connection duration controller, the presented system achieves effective and precise balancing performance that markedly outperforms passive voltage-equalizer techniques.

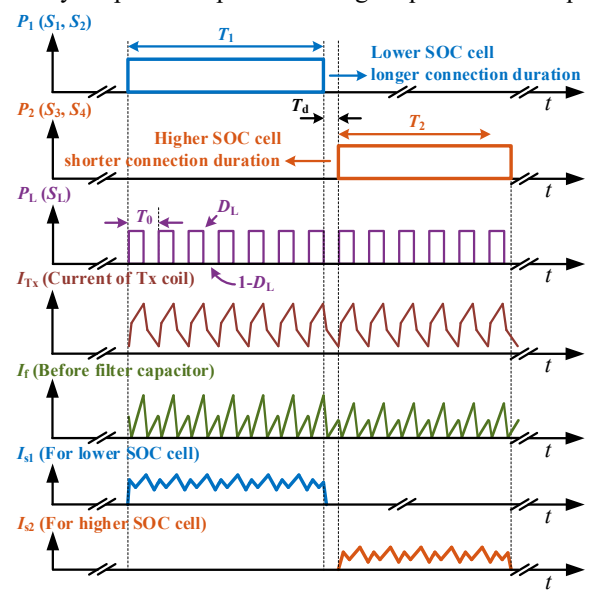


Fig. 9. Illustration of connection durations regulated by the controller and the key waveforms of the presented equalizer.

IV. EXPERIMENTAL RESULTS

To validate the presented IPT-based equalizer and the equalization control strategy, a scaled-down experimental prototype with five series-connected cells was developed in the laboratory, as depicted in Fig. 10.

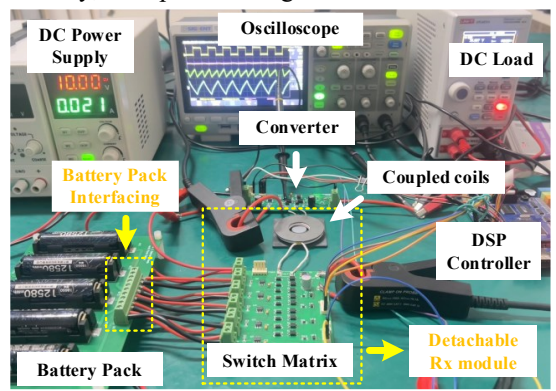


Fig. 10. Experimental prototype of the equalizer for five battery cells.

 $\label{thm:table III} The Specific Parameters of the Built Experimental Prototype$

Symbol	Description	Value
f_0	Converter switching frequency	200 kHz
$T_{ m f}$	Total cycle time for switch matrix	0.1 s
$V_{\mathrm{b}i}$	Voltage of the <i>i</i> -th battery cell	2.75-4.2 V
$V_{ m pack}$	Voltage of battery pack	13.75-21 V
$V_{ m Bus}$	Rated bus voltage of DC-DC converter	38 V
$V_{ m drop}$	The total voltage drop across the IPT loop	0.7 V
Q_{Cell}	Capacity of the utilized battery cell	3400 mAh
I_{C}	Reference battery pack charging current	1.7 A
R_{Load}	Nominal resistive load during discharging	$40~\Omega$
C_{F}	The capacitance of the filter capacitor	$22~\mu \mathrm{F}$
L_{Tx}	Inductance of Tx coil	$12.7~\mu\mathrm{H}$
L_{Rx}	Inductance of the Rx coils	$10 \mu \mathrm{H}$
k	Coupling coefficients between $L_{\rm Tx}$ and $L_{\rm Rx}$	0.82

The prototype utilizes a bidirectional, single-inductor DC–DC converter that handles both charging and discharging of the battery pack, employing IRLR120NTRPBF N-channel MOSFETs paired with SS56 Schottky diodes and all driven by the LM5109BMAX/NOPB gate driver. The QS5K2 dual N-channel common-source MOSFETs form the switch matrix and are also controlled by the same gate driver. The battery pack, consisting of five 18650-type lithium-ion cells in series (3.7 V nominal, 3400 mAh), is connected to the converter's right side. Depending on the operating mode, the converter's left side is connected either to a programmable DC electronic load (for discharge tests) or to a high-voltage DC source (for charging). Detailed specifications of the IPT-based equalizer are provided in Table III.

A. Discharging Experiment Results

During a rated discharging process, a DC electronic load with a resistance of 40 Ω is connected to the left side of the presented bidirectional single-inductor DC-DC converter.

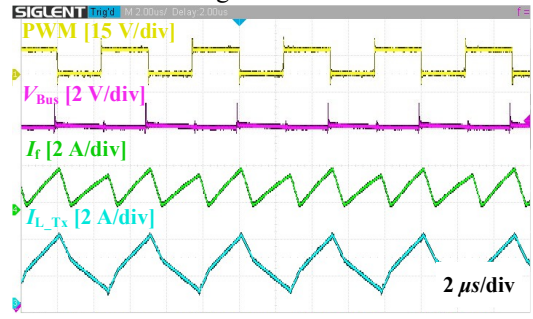


Fig. 11. Waveforms of the PWM signal for $S_{\rm H}$, output voltage $V_{\rm Bus}$, current $I_{\rm Tx}$, and feedback current $I_{\rm f}$ during discharging.

Fig. 11 illustrates the waveforms of the PWM signal for the high-side switch $S_{\rm H}$, the output voltage $V_{\rm Bus}$, the current $I_{\rm Tx}$ through the Tx coil $L_{\rm Tx}$, and the feedback current $I_{\rm f}$. The slope of $I_{\rm Tx}$ varies according to the operating states shown in Fig. 9, while the output voltage $V_{\rm Bus}$ follows the reference value and remains unaffected by the IPT process, which aligns with the theoretical analysis presented in Section III.

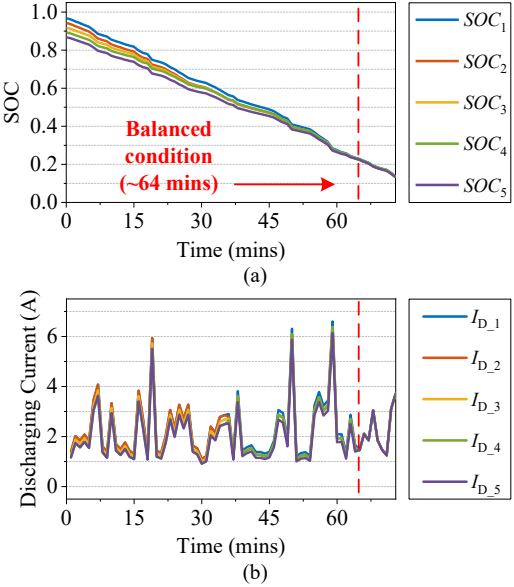


Fig. 12. Experimental balancing result of each battery cell in real load current discharging. (a) SOC values. (b) Discharging currents.

The balancing experimental results are presented in Fig. 12,

where the initial SOC values of the battery cells are 0.96, 0.935, 0.91, 0.885, and 0.86, respectively. To emulate realistic load dynamics, the discharging current follows a scaled-down profile derived from an electric aerial lift vehicle battery pack [31], [32], and is applied using a programmable DC electronic load. This current profile includes high-frequency and abrupt fluctuations, effectively reflecting real-world conditions.

The SOC values and discharging currents of each cell, as shown in Fig. 12(a) and Fig. 12(b), demonstrate that the equalizer effectively balances the SOC of the battery pack despite the dynamic variations in load current. The maximum SOC spread decreases from 10% to 0.5% within 64 mins, highlighting the equalizer's capability to achieve precise and robust balancing even under realistic discharge scenarios.

B. Charging Experiment Results

When a high-voltage power source is connected to the left side, the bidirectional single-inductor DC-DC converter operates in buck mode to charge the battery pack at a 0.5 C rate, i.e., 1.7 A. The waveforms of the PWM signal for the low-side switch S_L , the output voltage V_{Bus} , the current I_{Tx} through the Tx coil L_{Tx} , and the feedback current I_f are shown in Fig. 13. These waveforms are consistent with the expected shapes presented in Fig. 8, regardless of whether the system is in charging or discharging mode.

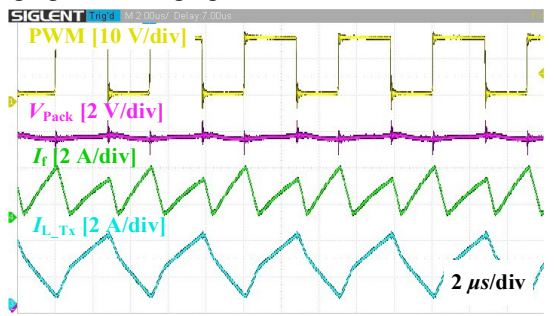


Fig. 13. Waveforms of the PWM signal for S_H , output voltage V_{Bus} , current I_{Tx} , and feedback current If during charging.

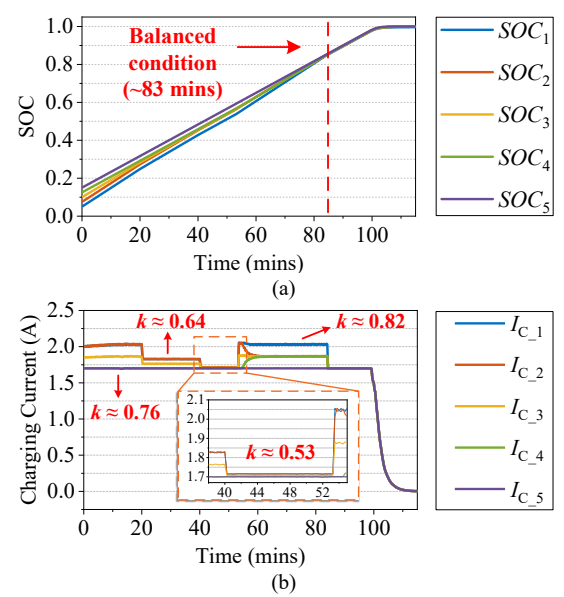


Fig. 14. Experimental balancing result of each battery cell under varying coupling conditions during charging. (a) SOC values. (b) Charging currents.

Furthermore, Fig. 14 illustrates the experimental results of the IPT-based equalizer during the charging process, where

the initial SOC values of the battery cells are 0.05, 0.075, 0.1, 0.125, and 0.15, respectively. To evaluate the system's performance under varying magnetic coupling conditions, the experiment introduces three representative levels of coil misalignment: slight (k = 0.76), moderate (k = 0.64), and severe (k = 0.53), in addition to the aligned condition (k =0.82) considered as the rated case.

As shown in Fig. 14, the shunt current decreases with weakening coupling and increases again once realignment is restored. Despite these variations, the equalizer effectively reduces the maximum SOC difference from 10% to 0.5% within 83 mins, demonstrating strong robustness against magnetic coupling changes. While a higher coupling coefficient enhances the balancing speed, it may also lead to greater power loss. In this article, the aligned condition is considered as the rated case to illustrate a fast and effective balancing performance. In practice, the rated coupling coefficient can be further optimized to meet specific application requirements.

C. Efficiency Analysis

Although the operational characteristics of the integrated bidirectional single-inductor DC-DC converter remain unaffected by the IPT process, its efficiency is significantly lower compared to conventional converters. To assess the impact of IPT on overall efficiency over the entire charging or discharging process, average efficiencies are employed here. During the balancing interval (from t_0 to t_B), the average efficiency of the IPT-based equalizer during discharging can be expressed as

$$\eta_{\rm D_BNg} = \frac{100\%}{t_{\rm B} - t_{\rm 0}} \int_{t_{\rm 0}}^{t_{\rm B}} \frac{V_{\rm Bus} I_{\rm Bus} + \sum_{i=1}^{n} I_{\rm si} V_{\rm bi}}{V_{\rm pack} I_{\rm pack}} dt.$$
 (27)

Similarly, the average charging efficiency during balancing is calculated as

$$\eta_{\text{C_BNg}} = \frac{100\%}{t_{\text{B}} - t_{0}} \int_{t_{0}}^{t_{\text{B}}} \frac{V_{\text{pack}} I_{\text{pack}} + \sum_{i=1}^{n} I_{\text{s}i} V_{\text{b}i}}{V_{\text{Bus}} I_{\text{Bus}}} dt \qquad (28)$$

where $V_{\rm bus}$ and $I_{\rm bus}$ denote the voltage and current in the left side of the presented equalizer, denote the pack voltage and current, and I_{si} and V_{bi} represent the shunt current and terminal voltage of the *i*-th battery cell.

It is worth to noting that when the system transitions to the balanced state, the feedback power $\sum_{i=1}^{n} I_{si} V_{bi}$ drops to zero, eliminating the power loss associated with the IPT process. Hence, the average efficiencies from t_B to t_E are simplified as

tee, the average efficiencies from
$$I_{\rm B}$$
 to $I_{\rm E}$ are simplified as
$$\eta_{\rm D_BEd} = \frac{1}{t_{\rm E} - t_{\rm B}} \int_{t_{\rm B}}^{t_{\rm E}} \frac{V_{\rm Bus} I_{\rm Bus}}{V_{\rm pack} I_{\rm pack}} dt \times 100\%. \tag{29}$$

$$\eta_{\rm C_BEd} = \frac{1}{t_{\rm E} - t_{\rm B}} \int_{t_{\rm B}}^{t_{\rm E}} \frac{V_{\rm pack} I_{\rm pack}}{V_{\rm Bus} I_{\rm Bus}} dt \times 100\%. \tag{30}$$

$$\eta_{\text{C_BEd}} = \frac{1}{t_{\text{E}} - t_{\text{B}}} \int_{t_{\text{E}}}^{t_{\text{E}}} \frac{V_{\text{pack}} I_{\text{pack}}}{V_{\text{Bus}} I_{\text{Bus}}} dt \times 100\%.$$
(30)

Fig. 15 presents the efficiency of the IPT-based equalizer under various pack power levels and operational modes. The experimental results show that improved efficiency in the balanced state, as the adaptive equalization algorithm halts the IPT process once the pack reaches balanced state. During charging, the efficiency at 40 W increases from 85.8 % (in the balancing state) to 91.5 % (in the balanced state), representing a 5.7 % absolute improvement. Similarly, for discharging, the efficiency increases from 84.3 % to 90.2 %, yielding a 5.9 % absolute gain at the same power level.

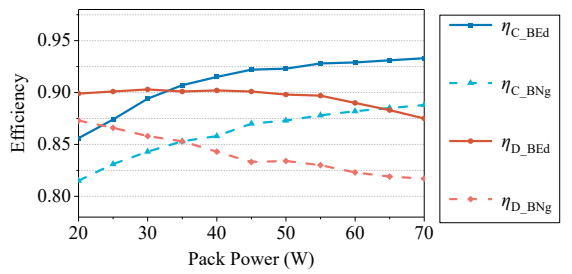


Fig. 15. Average efficiency of the introduced equalizer under varying pack power levels and operational modes.

Additionally, the observed difference in efficiency is due to lower switch voltage stress in buck mode (charging), resulting in reduced switching losses and higher efficiency.

During the charging process at a 0.5 C rate (pack current of 1.7 A), the system operates with a bus power of 36.23 W under balanced state and 38.5 W under balancing state. The average feedback current $I_{\text{f_ave}}$ is calculated as 1.05 A based on (20). According to the datasheets, the MOSFETs used have a conduction resistance of 185 m Ω , with rise and fall times of 35 ns and 22 ns, respectively. The DC resistances of the Tx and Rx coils are 0.46 Ω and 0.42 Ω , with rectifier and diode voltage drops of 0.7 V and 0.4 V, respectively.

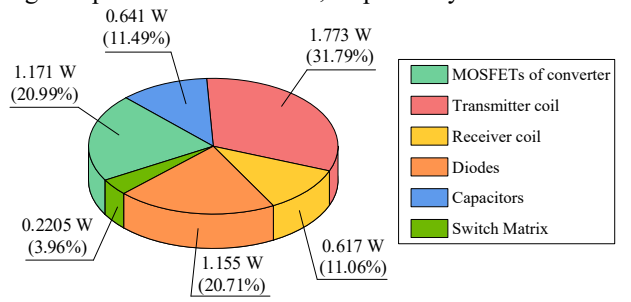


Fig. 16. Calculated power losses of the proposed system during $0.5\ \mathrm{C}$ charging operation.

Based on these parameters, the calculated power losses are: 1.171 W in converter MOSFETs, 1.155 W in the diodes, 0.221 W in capacitors, 1.773 W in the Tx coil, 0.617 W in the Rx coil, and 0.2205 W in the switch matrix. The calculated losses under the balancing state deviate by 4.6% from the measured values, and the deviation under the balanced state is 3.89%. Due to parasitic parameters and modeling simplifications, these errors are reasonable and acceptable. The summarized power losses of the presented equalizer are shown in Fig. 16.

V. ADDITIONAL COMMENTS

A. Parameter Tuning of Connection Duration Controller

As shown in Fig. 7(a), the adaptive equalization algorithm terminates the balancing process once the maximum SOC difference drops below the predefined threshold. To isolate and evaluate the dynamic response of the connection duration controller, the adaptive equalization algorithm is deactivated here, allowing investigation of equalization performance under different proportional-integral (PI) controller parameters.

 $\label{eq:table_iv} TABLE\ IV$ Different Control Parameters for The Results of Fig. 17

Figures	$K_{ ext{P-soc}}$	$K_{ ext{I-soc}}$	Balancing time
Fig. 17(a)	2.5	0.01	67 mins
Fig. 17(b) (Employed)	5.5	0.02	62.5 mins
Fig. 17(c)	11	0.06	62 mins

Fig. 17 illustrates the shunt currents and SOC values of the battery cells during 0.5 C charging under three different sets of PI parameters, which are detailed in Table III. The initial SOC values of Cell₁ to Cell₅ are set to 0.5, 0.75, 0.1, 0.125, and 0.15, respectively, with a maximum initial SOC error of 10%.

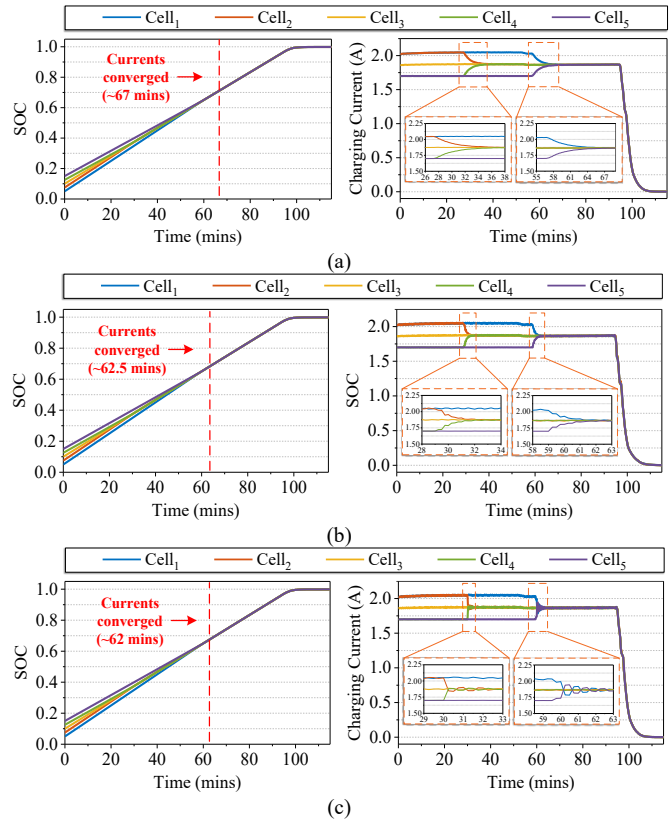


Fig. 17. Shunt current and SOC values for battery cells with different control parameters. (a) $K_{\text{P-soc}} = 2.5$ and $K_{\text{I-soc}} = 0.01$. (b) $K_{\text{P-soc}} = 5.5$ and $K_{\text{I-soc}} = 0.02$. (c) $K_{\text{P-soc}} = 11$ and $K_{\text{I-soc}} = 0.06$.

With smaller proportional and integral gains ($K_{P\text{-soc}} = 2.5$, $K_{\text{I-soc}} = 0.01$), as shown in Fig. 17(a), the controller exhibits a slower dynamic response, requiring approximately 67 mins to achieve convergence of the shunt currents. Increasing the gains to $K_{P\text{-soc}} = 5.5$ and $K_{\text{I-soc}} = 0.02$, as illustrated in Fig. 17(b), the balancing speed is significantly improved, reducing the convergence time to 62.5 mins while maintaining smooth and stable shunt current profiles. Further increasing the gains to $K_{P\text{-soc}} = 11$ and $K_{\text{I-soc}} = 0.06$, as depicted in Fig. 17(c), slightly reduces the balancing time to 62 mins, at the expense of introducing noticeable oscillations in the charging current due to the more aggressive control action.

It is worth noting that increasing the PI gains beyond the values shown in Fig. 17(b) does not significantly reduce the balancing time, mainly due to the saturation module limiting the connection duration controller. In summary, tuning the connection duration controller involves a trade-off between faster convergence and system stability. The parameters used in Fig. 17(b) strike an effective balance, enabling both rapid and stable SOC equalization.

B. Comparison of Different Balancing Strategies

Although a PI controller is utilized in the connection duration control scheme, it is necessary to compare it with other strategies to comprehensively evaluate the balancing performance under different equalization algorithms on the current experimental platform. As in Section V-I, the adaptive equalization algorithm is deactivated in this analysis to isolate the effects of the duration control strategies.

Three control strategies are implemented and tested on the same experimental platform: the introduced PI controller, a droop-inspired control, and a fixed-duration scheme, which represents a widely employed voltage-based balancing control [18]–[24]. The voltage-based approach relies on the negative relationship between the balancing current (shunt current) and the cell voltage, given as (21).

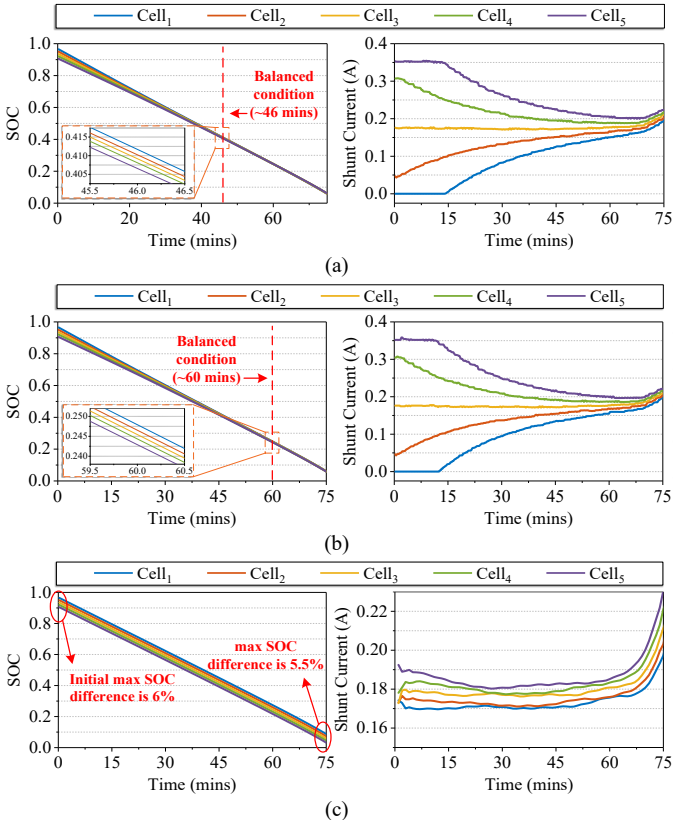


Fig. 18. Comparison of balancing performance under different connection duration control methods. (a) Employed PI controller ($K_{P-soc} = 1$, $K_{I-soc} = 0.01$). (b) Droop-inspired control. (c) Fixed-duration strategy.

To clearly highlight performance differences, the controller parameters are scaled down compared to those listed in Table III. Fig. 18 presents the SOC values and shunt currents of each cell under a constant load resistance of $40\,\Omega$ and a target bus voltage of 38 V. In which, the initial SOC values of the five cells are 0.965, 0.95, 0.935, 0.92, and 0.905, respectively, resulting in a maximum initial SOC deviation of 6%. Moreover, the balanced state is defined as a maximum SOC discrepancy within 0.5%.

As shown in Fig. 18(a), the employed PI-controlled method $(K_{P\text{-soc}} = 1, K_{I\text{-soc}} = 0.01)$ demonstrates the fastest convergence, achieving the balanced state within 46 minutes, while ensures smooth current transitions and maintains high balancing accuracy. The droop-inspired control (m=1), with its linear response to SOC deviation and lack of integral compensation, achieves balancing in 60 mins but converges slowly as the SOC differences further reduce. Meanwhile, the fixed-duration scheme exhibits markedly slower performance, reducing the initial SOC spread from 6% to only about 5.5% after 75 minutes. This limited effectiveness results from the

small voltage differences among cells with close SOC values and the flat voltage plateaus in the lithium-ion battery open-circuit voltage (OCV) curve [33], [34], both of which weaken the sensitivity and effectiveness of voltage-based balancing.

C. Trade-off Between Balancing and Efficiency

Replacing the conventional inductor in a bidirectional converter with a Tx coil enables wireless transfer of the coil's current ripple energy. Since the balancing rate scales with ripple amplitude, balancing capability can be boosted by either reducing the effective inductance of the Tx coil (hardware modification) or lowering the switching frequency of the introduced converter (software adjustment). Generally, the latter is preferred due to its greater implementation flexibility.

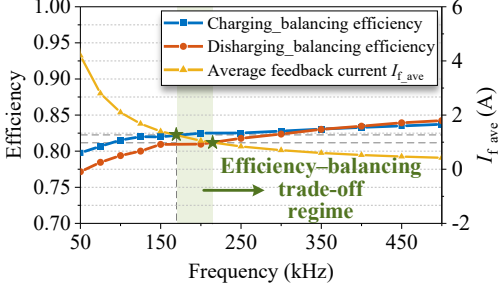


Fig. 19. Charging efficiency, discharging efficiency, and average feedback current $I_{\text{f ave}}$ as functions of converter's switching frequency.

However, indiscriminately reducing the switching frequency of employed converter is not advisable. As the frequency decreases, the current ripple grows, which can increase conduction losses and degrade overall converter performance. To identify the optimal operating range, the charging efficiency and discharging efficiency are measured and illustrated in Fig. 19, along with the average feedback current $I_{\rm f}$ ave calculated by (21).

As shown in Fig. 19, the frequency band between the intersections of the $I_{\rm f,ave}$ curve with the efficiency curves is defined as the efficiency–balancing trade-off region, which spans approximately 170 kHz to 210 kHz. Operating below this range prioritizes faster balancing but reduces efficiency, while operating above it improves efficiency at the cost of slower balancing. In this work, the switching frequency of 200 kHz is selected as a suitable compromise.

D. Potential for Bypass of Faulty Cells

In a typical series-connected battery pack, the failure of a single cell requires that cell to be electrically disconnected to prevent damage and ensure safety. However, once a faulty cell is cut off, the resulting open-circuit condition can interrupt the current path and disable the entire string, unless an alternative path is provided. In the original equalizer design (as shown in Fig. 2), an n-cell pack required only n drive signals by pairing adjacent MOSFET modules to share each gate drive. Specifically, switches S_{2i-1} and S_{2i} in the switch matrix are turned on simultaneously to connect Celli to the Rx circuit for balancing, which effectively reduces the overall cost and volume of system. However, this shared-signal design is incompatible with the fault bypassing control strategy for the switch matrix, and thus cannot support adequate bypassing.

To address this limitation, the improved equalizer integrates an exclusive gate driver for every switch module within the matrix. This configuration allows the corresponding bypass path to be controlled independently once a faulty cell has been disconnected. Hence, current can be rerouted through specific switches to maintain continuity for the remaining cells, effectively bypassing the failed cell without affecting overall pack operation. Fig. 20 illustrates four representative bypass configurations for a four-cell pack when one cell has been disconnected at different positions in the string. Moreover, Table V summarizes the switch pairs that need to conduct for an n-cell string, showing the potential to enhance system robustness under cell-level failure scenarios.

 $TABLE\ V$ Switch Pairs Required for Bypassing A Single Disconnected Cell.

Failed Cell Position	Conducting Switches
First cell $(i = 1)$	Cell ₁ & Cell ₃
Intermediate even-indexed Cell _i	$Cell_{2i} \& Cell_{2(i-1)}$
Intermediate odd-indexed Cell _i	$Cell_{2i-1}$ & $Cell_{2i+1}$
Last cell $(i = n)$	$\operatorname{Cell}_{2n} \& \operatorname{Cell}_{2(n-1)}$

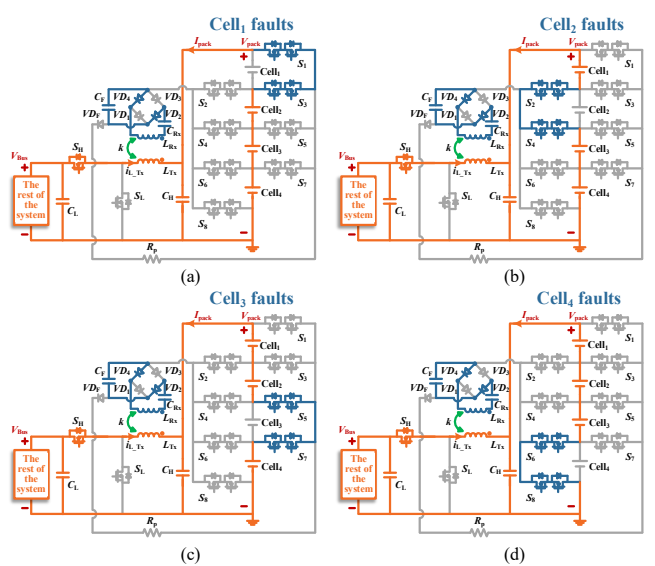


Fig. 20. Bypass configurations for different single-cell fault scenarios in a four-cell battery pack. (a) The first cell. (b) An intermediate even-indexed cell. (c) An intermediate odd-indexed cell. (d) The last cell.

E. Extension for Bidirectional SOC Balancing

In some applications, a power converter may connect to battery packs on both its input and output sides, as in energy storage systems, electric vehicles with auxiliary battery packs, or mobile charging stations. In such cases, simultaneous intrapack SOC balancing at both ends is often required, regardless of whether the packs are charging or discharging. Leveraging the modular design, the presented IPT-based equalizer can be readily extended to meet this demand.

As shown in Fig. 21, the system comprises three functional module types: the pack module, the balancing module, and the converter module. For bidirectional SOC balancing, each pack is equipped with its own balancing module, whose Rx coil is coupled to a larger Tx coil in the converter module, enabling effective intra-pack balancing on both sides.

At the software level, each pack module computes the SOC of its individual cells and their average value using coulomb counting, then transmits this data to its associated balancing module. Based on the received data, the balancing module regulates the conduction durations of each switch pairs to equalize that pack. Only minimal SOC data exchange between

corresponding modules is required, while the converter module maintains closed-loop control on output side.

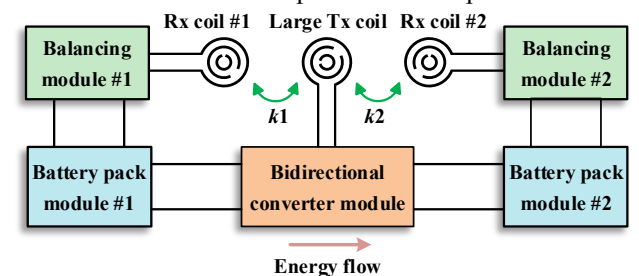


Fig. 21 Modular IPT-based equalizer for bidirectional SOC balancing

Moreover, the detachable design of the balancing module allows system size to be reduced when balancing is not needed, offering greater flexibility than transformer-based and other WPT/IPT-based equalizers.

F. Discussion on Ferrite Core Material Selection

In this work, a NiZn ferrite core is employed for the Tx coil, following the manufacturer's datasheet of the commercial component. However, at the operating frequency of 200 kHz, MnZn ferrite generally provides better performance than NiZn due to its higher permeability and lower core loss in this frequency range [37], [38].

It should be noted that the primary focus of this work is the balancing topology and SOC equalization control strategy, which are largely independent of the specific ferrite material used. Nevertheless, future work will focus on the influence of magnetic material selection on efficiency, thermal behavior, and system performance to support further improvement and optimization for practical applications.

VI. COMPARISON WITH SIMILAR EXISTING EQUALIZERS

In Table VI, different transformer-, WPT-, and IPT-based battery equalizers are compared in terms of AC power reliance, inverter usage, voltage multiplier adoption, balancing strategy, and efficiencies in both charging and discharging modes. For some active balancing methods, the BNg indicates the balancing state while the BEd denotes the balanced state. The VMs are incorporated to enhance voltage levels for cell balancing in [21]-[24]. However, this approach inherently introduces conversion losses and increased component stress, leading to relatively low efficiencies of 72.8% to 76.8%. Additionally, in [25] the switch matrix is embedded directly in the main charging path, resulting in a balancing efficiency of 60.3%. By contrast, in the proposed method, the switch matrix is placed in the auxiliary balancing circuit, where the current is relatively low, contributing to only 3.96% of the total power loss and thereby maintaining high overall efficiency.

Ref. [18]–[24] benefit from simple control methods, such as automatic or voltage-based control, but these are insufficient for applications requiring high balancing accuracy. In contrast, systems with active and precise control strategies, such as the switch matrix-based equalizer in [25] and the SOC-based method proposed in this work, achieve higher balancing accuracy at the cost of increased control complexity. It is worth noting that the employed switch matrix features moderate control complexity, as it only adjusts the connection duration of each cell instead of requiring precise real-time current regulation as in [27]. This trade-off ensures a balance

TABLE VI COMPARISON OF WIRELESS POWER TRANSFER- AND INDUCTIVE POWER TRANSFER-BASED BATTERY EQUALIZER

Battery Balancing methods	AC Power	AC Power Inverter Voltage Switch Balancing Reliance Reliance Multiplier Matrix Strategy		Switch	Balancing	Control	Efficiency		
Battery Balancing methods	Reliance			Complexity	Charging	Discharging			
Transformer-Based Equalizer [18]	No	No	No	No	Automative	Low	94.2%	93.6%	
Multiple-Receiver WPT Equalizer [19]	Yes	No	No	No	Automative	Low	74.5%	N/A	
Voltage Doubler IPT Equalizer [20]	No	Yes	No	No	Voltage-Based	Moderate	80%	N/A	
Scalable Cell-String WPT Equalizer [21]	Yes	No	Yes	No	Automative	Low	76.5%	N/A	
Anti-Misalignment WPT Equalizer [22]	No	Yes	Yes	No	Voltage-Based	Middle	76.8%	N/A	
Low-Cost WPT Equalizer [23]	Yes	No	Yes	No	Automative	Low	72.8%	N/A	
Hybridized Ad-Hoc Wireless Charger [24]	No	Yes	Yes	No	Voltage-Based	Moderate	BNg: 76.4% BEd: 88.6%	N/A	
C 'A I M A ' D A I WINTER I' 1961	N	37	N	37	W to D 1	TT: 1	BEd: 88.6% BNg: 60.3%	N T/A	
Switch Matrix-Based WPT Equalizer [25]	No	Yes	No	Yes	Voltage-Based	High	BEd: 84.2%	N/A	
WPT-Based Modular Equalizer [26]	No	Yes	No	No	Voltage-Based	High	N/A	N/A	
WPT Discharging Equalizer [27]	No	No	No	No	SOC-Based	High	N/A	BNg: 68.3%	
WF1 Discharging Equalizer [27]	NO	110	NO	NO	SOC-Dased	mgn	IN/A	BEd: 87.6%	
This Paper	No	No	No	Yes	SOC-Based	Moderate	BNg: 85.8%	BNg: 84.3%	
Tills Laper	110	110	110	1 68	SOC-Based	Moderate	BEd: 91.5%	BEd: 90.2%	

BNg indicates the balancing state and BEd indicates the balanced state.

TABLE VII
COMPARISON OF COMPONENT COUNTS AND OVERALL COST IN BATTERY EQUALIZERS FOR SIX CELLS (THREE MODULES)

Battery Balancing methods	Transformer	Diode	MOSFETs	Common source MOSFETs	Switches Driver	Inductor	Capacitor	Coil	Cost
Transformer-Based Equalizer [18]	1	6	2	0	2	0	2	0	\$21.8
Multiple-Receiver WPT Equalizer [19]	0	24	5	0	5	3	15	7	\$25.3
Voltage Doubler IPT Equalizer [20]	0	6	4	0	4	1	8	4	\$28.6
Scalable Cell-String WPT Equalizer [21]	0	12	4	0	4	1	10	4	\$30.4
Anti-Misalignment WPT Equalizer [22]	0	18	4	0	4	1	11	5	\$36.9
Low-Cost WPT Equalizer [23]	0	12	5	0	5	2	11	2	\$22.7
Hybridized Ad-Hoc Wireless Charger [24]	0	12	8	0	8	2	13	2	\$26.3
Switch Matrix-Based WPT Equalizer [25]	0	4	12	9	21	1	7	2	\$34.0
WPT-Based Modular Equalizer [26]	0	0	24	0	24	6	13	12	\$93.9
WPT Discharging Equalizer [27]	0	30	8	0	8	0	15	7	\$53.5
This Paper	0	4	2	12	8	0	3	2	\$21.5

Note: Costs calculated for a quantity of 100 units.

between control simplicity and performance, making it a practical choice for WPT-based battery equalization.

Table VII provides a quantitative comparison of component counts and costs for several six-cell (three-module) equalizer implementations. Key components include multi-winding transformers (\$18.00 each), diodes (\$0.20 each), N-channel MOSFETs (\$0.50 each), integrated common-source N-channel MOSFETs (\$0.40 each), drivers (\$0.50 each), fixed inductors (\$1.00 each), capacitors (\$0.30 each), and coils (\$5.00 each), all based on pricing for 100-unit orders.

Among these, the presented IPT-based equalizer achieves the lowest total cost of \$21.50. This cost advantage is attributed to the utilization of a single shared Rx circuit with adaptive connection duration control, enabling accurate SOC balancing while minimizing component count. The integrated common-source MOSFETs further reduce cost by operating under lower voltage and current stresses, allowing the use of lower-rated and more economical devices.

In contrast, transformer-based designs such as [18] are typically custom-designed and require fully symmetrical multi-winding transformers to ensure balancing accuracy, which leads to considerable manufacturing challenges [35]. Therefore, a unit price of \$18.00 is reasonably adopted in this comparison considering the associated customization and

manufacturing requirement.

While [18] does not report the volume information, the transformer volume is estimated to be 9.52 cm³ based on its predecessor work [36] for six cells. This is slightly smaller than the 11.61 cm³ volume of the coils used in the IPT-based design. However, transformer volume scales with the number of cells, as each cell requires an exclusive secondary winding. In contrast, the Rx coil in IPT-based designs is shared and remains constant regardless of the cell count. Thus, for larger battery systems, the IPT-based equalizer offers not only better cost efficiency but also greater scalability in volume.

VII. CONCLUSION

In this study, an IPT-based equalizer is presented to achieve efficient battery equalization during both charging and discharging, enhancing its practical applicability. The equalizer utilizes a bidirectional single-inductor DC-DC converter, in which the inductor is replaced by an equivalent impedance Tx coil. A single Rx coil wirelessly captures feedback energy, effectively addressing cross-coupling issues and avoiding parameter inconsistency. Experimental results validate the capability of the presented equalizer to balance the battery pack and confirm the feasibility of the introduced battery balancing controller during both charging and

discharging, even under real discharging scenarios and varying coupling coefficients. Furthermore, efficiency analysis reveals significant improvements with the introduced efficient adaptive equalization algorithm, showing a 5.9 % gain during discharging and a 5.7 % improvement during charging. Moreover, the integration of a switch matrix allows for cell-level fault isolation and mitigates cross-coupling issues within the battery system, thereby significantly enhancing the system's operational reliability and balancing performance.

REFERENCES

- [1] S. Wang, Y. Wang, G. Chen, D. Wei, and Y. Shang, "An Efficient and Compact Equalizer Based on Forward-Flyback Conversion for Large-Scale Energy Storage Systems," *IEEE Trans. Transport. Electrific.*, vol. 10, no. 1, pp. 1222–1232, Mar. 2024.
- [2] M. A. Hannan, M. M. Hoque, S. E. Peng, and M. N. Uddin, "Lithium-Ion Battery Charge Equalization Algorithm for Electric Vehicle Applications," *IEEE Trans. on Ind. Applicat.* vol. 53, no. 3, pp. 2541– 2549, May. 2017.
- [3] D. Ansean, M. Gonzalez, V. M. Garcia, J. C. Viera, J. C. Anton, and C. Blanco, "Evaluation of LiFePO4 batteries for Electric Vehicle applications," *IEEE Trans. on Ind. Applicat.*, vol. 51, no. 2, pp. 1855–1863, Mar. 2015.
- [4] F. Liu, R. Zou, Y. Liu, and Y. Wang, "A Modularized Voltage Equalizer Based on Phase-Shift Modulation for Series-Connected Battery Strings," *IEEE Trans. Ind. Electron.*, vol. 70, no. 12, pp. 12 475–12 485, Dec. 2023.
- [5] M. K. Al-Smadi and J. A. A. Qahouq, "Evaluation of Current-Mode Controller for Active Battery Cells Balancing With Peak Efficiency Operation," *IEEE Trans. Power Electron.*, vol. 38, no. 2, pp. 1610–1621, Feb. 2023.
- [6] Y. Shang, B. Xia, C. Zhang, N. Cui, J. Yang, and C. C. Mi, "An Automatic Equalizer Based on Forward–Flyback Converter for Series-Connected Battery Strings," *IEEE Trans. Ind. Electron.*, vol. 64, no. 7, pp. 5380–5391, Jul. 2017.
- [7] N. Ghaeminezhad, Q. Ouyang, X. Hu, G. Xu, and Z. Wang, "Active Cell Equalization Topologies Analysis for Battery Packs: A Systematic Review," *IEEE Trans. Power Electron.*, vol. 36, no. 8, pp. 9119–9135, Aug. 2021.
- [8] W. Liu et al., "Distributed Voltage Equalization Design for Supercapacitors Using State Observer," *IEEE Trans. Ind. Appl.*, vol. 55, no. 1, pp. 620–630, Jan. 2019.
- [9] M.-Y. Kim, C.-H. Kim, J.-H. Kim, and G.-W. Moon, "A Chain Structure of Switched Capacitor for Improved Cell Balancing Speed of Lithium-Ion Batteries," *IEEE Trans. Ind. Electron.*, vol. 61, no. 8, pp. 3989–3999, Aug. 2014.
- [10] X. Guo, Q. Wu, C. Xing, W. Qian, and Y. Zhao, "An active equalization method for series-parallel battery pack based on an inductor," *J. Energy Storage*, vol. 64, p. 107157, Aug. 2023.
- [11] W. Lujun et al., "Efficient and Fast Active Equalization Method for Retired Battery Pack Using Wide Voltage Range Bidirectional Converter and DBSCAN Clustering Algorithm," *IEEE Trans. Power Electron.*, vol. 37, no. 11, pp. 13 824–13 833, Nov. 2022.
- [12] G. Noh, J. Lee, and J.-I. Ha, "Design and Analysis of Single-Inductor Power Converter for Both Battery Balancing and Voltage Regulation," *IEEE Trans. Ind. Electron.*, vol. 69, no. 3, pp. 2874–2884, Mar. 2022.
- [13] Y. Ye, J. Wang and X. Wang, "A Multi-Winding Transformer-Based Active Cell Equalizer with Self-Driven Switches for Series-Connected Lithium-Ion Batteries and Super-Capacitors," *J. Energy Storage*, vol. 70, p. 107971, Oct. 2023.
- [14] S. Li, C. C. Mi, and M. Zhang, "A High-Efficiency Active Battery-Balancing Circuit Using Multi-Winding Transformer," *IEEE Trans. Ind. Appl.*, vol. 49, no. 1, pp. 198–207, Jan. 2013.
- [15] C.-S. Lim, K.-J. Lee, N.-J. Ku, D.-S. Hyun, and R.-Y. Kim, "A Modularized Equalization Method Based on Magnetizing Energy for a Series-Connected Lithium-Ion Battery String," *IEEE Trans. Power Electron.*, vol. 29, no. 4, pp. 1791–1799, Apr. 2014.
- [16] Y. Shang, N. Cui, and C. Zhang, "An Optimized Any-Cell-to-Any Cell Equalizer Based on Coupled Half-Bridge Converters for Series-Connected Battery Strings," *IEEE Trans. Power Electron.*, vol. 34, no. 9, pp. 8831–8841, Sep. 2019.

- [17] Y. Li, J. Xu, X. Mei, and J. Wang, "A Unitized Multiwinding Transformer-Based Equalization Method for Series-Connected Battery Strings," *IEEE Trans. Power Electron.*, vol. 34, no. 12, pp. 11981– 11989, Dec. 2019.
- [18] B. Xu et al., "A Double-Switch Single-Transformer Integrated Equalizer for the Recycled Power Battery String of Automatic Guided Vehicles," *IEEE Trans. Ind. Electron.*, vol. 70, no. 3, pp. 2596–2606, Mar. 2023.
- [19] M. Liu, M. Fu, Y. Wang, and C. Ma, "Battery Cell Equalization via Megahertz Multiple-Receiver Wireless Power Transfer," *IEEE Trans. Power Electron.*, vol. 33, no. 5, pp. 4135–4144, May. 2018.
- [20] L. Liu et al., "A Multiple-Receiver-IPT-Based Voltage Equalizer With Voltage Doublers for Battery-String Charging," in *IEEE J. Emerging Sel. Top. Power Electron.*, vol. 13, no. 1, pp. 1339-1348, Feb. 2025.
- [21] P. Zhang et al., "Wireless Power Transfer-Based Voltage Equalizer for Scalable Cell-String Charging," *IEEE Trans. Ind. Electron.*, vol. 71, no. 1, pp. 493–503, Jan. 2024.
- [22] P. Zhang et al., "Dual-Layer Equalization Architecture for Anti-Misalignment Capability Enhancement in Multiple-Receiver-Based WPT Equalizer," *IEEE Trans. Power Electron.*, pp. 1–12, 2024.
- [23] M. Fu, C. Zhao, J. Song, and C. Ma, "A Low-Cost Voltage Equalizer Based on Wireless Power Transfer and a Voltage Multiplier," *IEEE Trans. Ind. Electron.*, vol. 65, no. 7, pp. 5487–5496, Jul. 2018.
- [24] P. Zhang et al., "Wireless Charging of Large-Scale Energy Storage Systems: A Hybridized Ad-Hoc Approach for High Efficiency," *IEEE Trans. Power Electron.*, vol. 38, no. 11, pp. 13 374–13 383, Nov. 2023.
- [25] J. Sun et al., "A novel charging and active balancing system based on wireless power transfer for Lithium-ion battery pack," J. Energy Storage, vol. 55, p. 105741, 2022.
- [26] D. Zheng et al., "Research on Battery Module Equalization Strategy for Wireless Power Transfer System," in Proc. Int. Conf. Power Energy Syst. Appl., 2023, pp. 139–143.
- [27] Y. Cao, Y. Liao, L. Chen, C. Wang and Y. Hu, "A Wireless Power Feedback-Based Battery Equalizer with Multiple-Receiver," in *IEEE Trans. Transp. Electrif.*, vol. 11, no. 4, pp. 9332-9345, Aug. 2025.
- [28] X. He, C. Zhu, J. Tao, Y. Zhang, and R. Mai, "Analysis and Design of a Cost-Effective WPT System With Single-Input and Multioutput Based on Buck-Integrated Rectifier," *IEEE Trans. Power Electron.*, vol. 38, no. 10, pp. 12 388–12 393, Oct. 2023.
- [29] M. Uno and K. Tanaka, "Single-Switch Multioutput Charger Using Voltage Multiplier for Series-Connected Lithium-Ion Battery/Supercapacitor Equalization," *IEEE Trans. Ind. Electron.*, vol. 60, no. 8, pp. 3227–3239, Aug. 2013.
- [30] Y. Cao and J. A. Abu Qahouq, "Analysis and Evaluation of a Dual-Variable Closed-Loop Control of Power Converter With Wireless and Nonwireless Power Transfer," *IEEE Trans. Ind. Electron.*, vol. 66, no. 4, pp. 2668-2679, Apr. 2019.
- [31] C. Wang, R. Li, Y. Cao, and M. Li, "A hybrid model for state of charge estimation of lithium-ion batteries utilizing improved adaptive extended Kalman filter and long short-term memory neural network," *J. Power Sources*, vol. 620, p. 235272, Nov. 2024.
- [32] C. Wang, F. Li, Y. Liao, and Y. Cao, "Flyback converter based charge balancing control with cell-load and cell-cell operation modes in battery system," *Appl. Energy*, vol. 394, p. 126181, Sept. 2025.
- [33] X. Cui, W. Shen, Y. Zhang, C. Hu, and J. Zheng, "Novel active LiFePO4 battery balancing method based on chargeable and dischargeable capacity," *Comput. Chem. Eng.*, vol. 97, pp. 27–35, Feb. 2017.
- [34] Y. Wang, C. Zhang, Z. Chen, J. Xie, and X. Zhang, "A novel active equalization method for lithium-ion batteries in electric vehicles," *Appl. Energy*, vol. 145, pp. 36–42, May 2015.
- [35] W. Huang and J. A. A. Qahouq, "Energy Sharing Control Scheme for State-of-Charge Balancing of Distributed Battery Energy Storage System," *IEEE Trans. Ind. Electron.*, vol. 62, no. 5, pp. 2764–2776, May 2015.
- [36] L. Liu et al., "A Low-Cost Multiwinding Transformer Balancing Topology for Retired Series-Connected Battery String," IEEE Trans. Power Electron., vol. 36, no. 5, pp. 4931–4936, May 2021.
- [37] Z. Li *et al.*, "Microstructure, magnetic properties, and loss performance of the Cu-substituted MnZn ferrites," *Ceram. Int.*, vol. 49, no. 24, pp. 40275–40283, Dec. 2023.
- [38] P. Andalib and V. G. Harris, "Grain boundary engineering of power inductor cores for MHz applications," *J. Alloys Compd.*, vol. 832, p. 153131, Aug. 2020.